

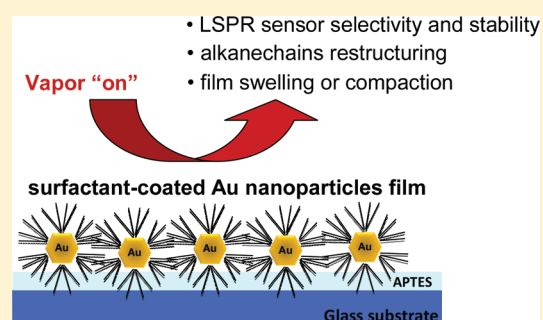
Improved Vapor Selectivity and Stability of Localized Surface Plasmon Resonance with a Surfactant-Coated Au Nanoparticles Film

María C. Dalfovo, Roberto C. Salvarezza, and Francisco J. Ibañez*

Instituto de Investigaciones Fisicoquímicas, Teóricas y Aplicadas (INIFTA), Universidad Nacional de La Plata - CONICET, Sucursal 4 Casilla de Correo 16 (1900), La Plata, Argentina

Supporting Information

ABSTRACT: Here, we report the use of tetraoctylammonium bromide (TOABr)-coated Au nanoparticles (NPs) for the optical sensing of volatile organic compounds (VOCs). We find that the film responded selectively to the presence of polar and nonpolar vapors by changes in the maximum wavelength (λ_{\max}) toward higher and lower wavelengths, respectively, as determined by UV–visible spectroscopy. We also observed that the organic coating reorganizes when vapors partition into the film indicated by FT-IR and the film contracts in the presence of water indicated by scanning electron microscopy (SEM). In the present sensor, the metallic Au core serves as the plasmonic signal while the organic coating acts as the receptor material providing vapor selectivity and sensor stability. Correlating changes in (λ_{\max}) with changes in the refractive index (RI) and nanoparticle-to-nanoparticle separation in the film is important both fundamentally and for improving selectivity in localized surface plasmon resonance (LSPR) sensors.



The localized surface plasmon resonance (LSPR) is a surface phenomenon induced by incident light on the oscillating frequency of electrons confined on a metallic nanostructure. When the frequency between incident light and plasmon match each other, a maximum extinction peak (absorbance + scattering) occurs at a wavelength (λ_{\max}) characteristic of the metal composition.¹ The extinction peak is sensitive to changes either in the bulk refractive index (RI)² or to local binding of molecules on specific surface sites known as “hot-spots.”^{3,4} A fair amount of work has been reported on the use of metal nanostructures for molecular and biomolecular LSPR sensing.^{5–7} In general, great efforts have been put through to improve sensitivity in LSPR sensors as demonstrated for the size,⁸ metal composition (Au⁹ vs Ag¹⁰ spheres), nanostructure conformation (core–shell or hallow),⁹ aspect ratio,^{10–12} and shape.^{10,13} Since the appearance of nanorods¹⁴ or elongated structures,¹⁵ researchers have shown that longitudinal plasmons are more sensitive than transversal ones.¹¹ Others have selectively attached biomolecules¹⁶ demonstrating that sensitivity relies upon the distance between the analyte and the plasmonic surface.^{17,18}

LSPR studies based on interparticle distance-dependence plasmon coupling effects have been less explored.^{19–23} On the basis of the distance between nanostructures and polarization of light,²² they may enter attractive or repulsive electromagnetic coupling (dipole–dipole interaction) leading to higher or lower energy shift.²⁰ Some examples include silica-coated Au nanoparticles (NPs),¹⁹ Au NPs separated by lithography,²² Au nanodiscs,²⁰ and a thin Au NPs film later functionalized with various alkanethiol chain length self-assembled monolayers (SAMs).²³ It has been shown that, as long as nanoparticle

distance decreases, there is a noticeable shift toward higher wavelengths (lower energy) and vice versa. The shift toward red or blue allows one to indirectly characterize the interparticle distance and their interactions.²⁴ Most of those experiments, however, usually require tedious syntheses and 2D assemblies along with costly instrumentation such as the use of a clean room facility for photolithography.

The optical detection of molecules in the gas^{25,26} and vapor phase^{27,28} is important in areas ranging from environmental concerns to medical diagnostics. Just recently, Liu et al.²⁵ reported the detection of H₂ gas by elegantly placing a single Au nanoantenna in proximity to a Pd nanostructure whose PdH_x formation was detected by changes in the Au plasmon. Van Duyne and co-workers²⁶ detected extremely low concentrations of inert gas and humid air with Ag and Au nanosphere films. They demonstrated that films responded distinctly to a 1/10 000 difference in refractive index value between Ar and He gas. Lu and co-workers built a LSPR sensor array comprised of Ag and Au NPs, and Au nanoshell films later functionalized with decanethiol, naphthalene thiol, and 2-mercaptobenzothiolate in order to improve selectivity toward various volatile organic compounds (VOCs).²⁸ Another group improved selectivity by placing hydrophobic and hydrophilic polymers on top of Au NP films whose RI changed on the basis of the affinity between the vapor analyte and the polymer.²⁹ So far, the majority of sensors focused on sensitivity issues while

Received: February 19, 2012

Accepted: May 3, 2012

Published: May 3, 2012

selectivity and stability still remain challenging because the extinction peak usually red shifts in the presence of different analytes²⁷ and naked nanoparticles (NPs) are prone to air oxidation.³⁰

Chemically modified metal NPs further assembled as films have been rarely applied in LSPR sensing.^{27,31} It is known that strong ligands such as alkanethiols modify the RI and drastically damp the plasmon signal by withdrawing electrons from the metal surface.³² This issue may have prevented the use of organic-coated metal NP films for LSPR sensing. The opposite occurs in chemiresistors,^{33,34} where organic-modified metal NPs are required for detecting changes in the film resistance upon the presence of vapor analytes^{35,36} via changes in the electron hopping conductivity.³⁷ It has been demonstrated that chemiresistive films swell in the presence of vapors in which they are soluble, and in fewer cases, the film contracts upon vapors of different polarity leading to an increase^{35,38} or decrease³⁸ in distance between NPs, respectively.

The organic material surrounding the nanoparticles not only provides stability to the film but also functions as a receptor element for incoming vapor molecules. To the best of our knowledge, changes in the Fourier transform infrared spectroscopy (FT-IR) caused by the presence of vapor-phase analytes have been so far unexplored. A shift in the vibration frequency to lower or higher energy, observed in the FT-IR experiments, provides qualitative information about the alkane chain organization surrounding the nanoparticle.³⁹ Organization depends on the few variables including the chemical nature of the ligands,^{40,41} nanoparticle size and composition, and dielectric of the medium. It has been shown that longer and strongly^{40,42} bounded alkane chains (i.e., mercaptans) assemble on Au surfaces in a well-organized fashion better than shorter and less-strongly⁴¹ physisorbed ligands. A higher alkyl chain order is generally attributed to van der Waals interactions.

In the present work, we obtained tetraoctylammonium bromide (TOABr)-coated Au nanoparticles (SNPs) through a simple benchtop synthesis, assembled them in a 3D film, and later used them for sensing. The organic chain acts as a molecular ruler providing a well-controlled distance between nanoparticles. We find that the film responded selectively by changes in the maximum wavelength (λ_{\max}) toward blue and red when exposed to headspace toluene (Tol) and ethanol (EtOH) vapors, respectively, as determined by UV-visible spectroscopy (UV-vis). Changes to blue are attributed to an interparticle separation (film swelling) while changes to red correspond to a cooperation between an increase in RI and film compaction (or interparticle distance decrease). Interestingly, the organic coating reorganizes when vapors partition into the film indicated by changes in the asymmetric CH_2 stretching vibration toward higher and lower wavenumbers. The use of scanning electron microscopy (SEM) indicates that the film contracts in the presence of water, and atomic force microscopy (AFM) shows film thinning upon Tol vapor. We also compare SNPs with citrated-coated Au NPs (CNPs) and dodecanethiol Au monolayer-protected clusters (C12S Au MPCs) in LSPR and FT-IR experiments, respectively. We also demonstrate that citrate-coated Ag NPs (Ag CNPs) films are instable in air. Finally, a single TOABr-coated Au film is selective toward various VOCs, stable over long periods of time, and easily assembled on substrates for LSPR and FT-IR sensing experiments.

■ EXPERIMENTAL SECTION

Synthesis. The TOABr-coated Au NPs (SNPs) were synthesized according to the two-phase Brust-Schiffrin reaction but without the addition of mercaptans.⁴³ Briefly, 0.71 mL of 25 mM HAuCl_4 was dissolved in 25 mL of water, and 0.012 g of TOABr was dissolved in 50 mL of toluene. The two solutions were combined and stirred until all of the AuCl_4^- transferred into the toluene phase. The solution turned a dark wine red after a 10-fold excess of NaBH_4 with respect to Au was added to the toluene solution with stirring. The SNPs prepared in this manner are 4.39 ± 1.25 nm based on transmission electron microscopy (TEM) (Figure S1, Supporting Information). Citrate-coated Au⁴⁴ (CNPs) and Ag NPs (Ag CNPs) and dodecanethiol Au monolayer-protected clusters (C12 Au MPCs)⁴⁵ were synthesized using known protocols and used as a comparison in this work.

Film Deposition. The as-synthesized NPs were assembled on aminopropyl-triethoxysilane (APTES)-modified glass substrate by immersion into the SNPs solution for 20 h. UV-vis and FT-IR experiments were performed on solid-state films by exposing them to headspace vapors of Tol and EtOH run in dry air (background) and ambient air. Microscopy data including AFM, SEM, and TEM images were taken from as-prepared films and drop-cast films deposited from a Tol + water mixture (See Experimental Details in Supporting Information).

Film Characterization. AFM, TEM, and SEM images were acquired with a Veeco Digital Instruments Nanoscope V (Santa Barbara, CA) using a Si tip operating in tapping mode, a FEI CM200 UT operated at 200 keV, and a FEI QUANTA 200 between 15 and 20 keV, respectively.

Sensing. LSPR measurements were taken in humid and dry atmosphere and acquired on a UV-vis Perkin-Elmer Lambda 35 spectrophotometer in a wavelength range between 300 and 900 nm. Since plasmon changes are small, it becomes difficult to analyze the actual UV-vis plot. Therefore, all the samples involved in this study were analyzed by comparing the actual UV-vis plots and by exporting raw data in the form of rows and columns as shown in Table S1, Supporting Information. In addition, we compared those values with the λ_{\max} generated by the software. In all cases, measurements matched up. We noticed that SNPs are quite sensitive to humidity (Table S2, Supporting Information) present in the normal experimental conditions and decided to expose these films to EtOH and Tol vapors using dry air as a background. This was achieved by keeping silica gel inside the UV-vis compartment during the entire run. The sample was resting 10 min along with the silica gel before a vial containing the solvent of interest (vapor source) was placed inside the compartment. Measurements were taken every 90 s during a total 15 min vapor exposure. The vial containing the solvent was removed, and the compartment door opened to ambient air for 450 s while keeping the desiccant inside. The maximum plasmon shift (λ_{\max}) reported here is obtained from 10 measurements during vapor exposure. FT-IR measurements were acquired on a PIKE Miracle Varian 600 Instrument in transmission mode following the same sample preparation; however, a thicker film was needed in order to improve the signal of the instrument. Assembled films were further drop-casted with 3 drops containing 5 μL from a 1.1 mg/ μL NP solution.

RESULTS AND DISCUSSION

LSPR Sensing. Figure 1a shows an actual UV–vis plot for a selected SNP film exposed to dry air and headspace vapors of EtOH and Tol, as indicated. Figure 1b shows the maximum plasmon change (λ_{\max}) taken from a pool of three SNP films exposed to the same headspace vapors run in dry air (baseline or background gas) over 270 s (see Table S2, Supporting Information). The figure reveals that the films respond with

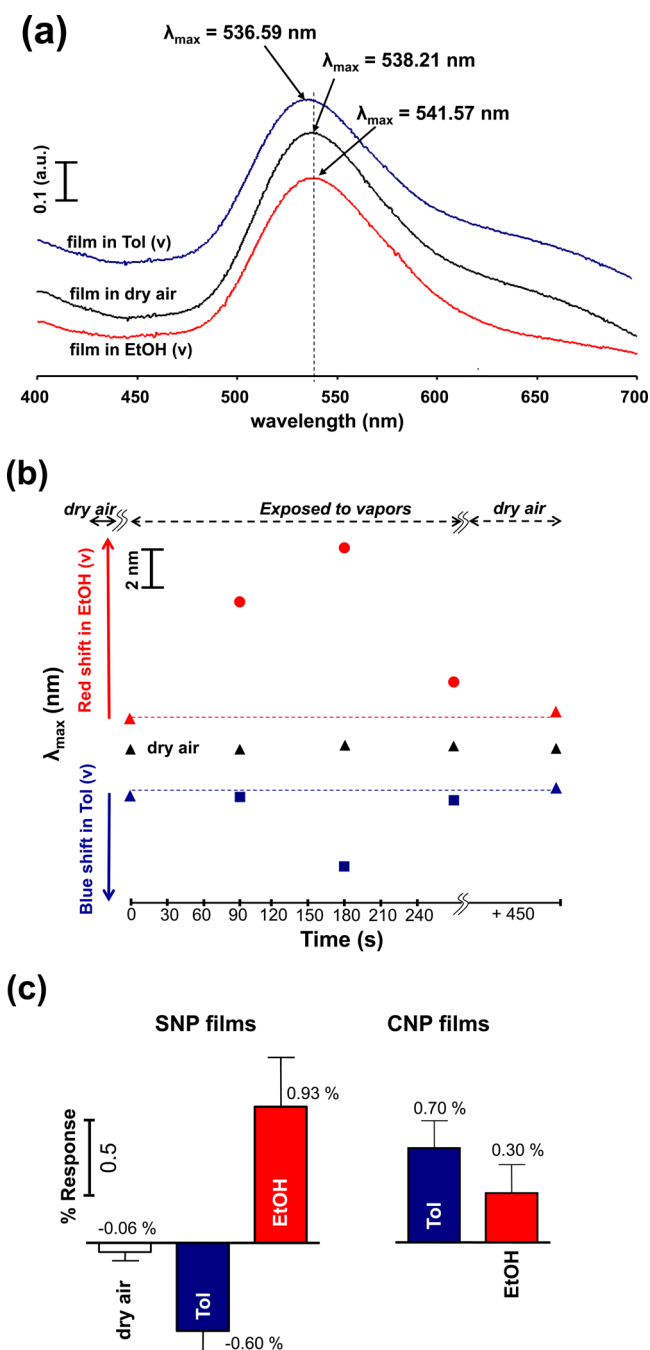


Figure 1. (a) Actual UV–vis plot showing the maximum plasmon change (λ_{\max}) from a selected SNPs film, (b) plot of maximum plasmon change (λ_{\max}) vs time (s) from SNP samples, and (c) bar chart shows an average percent response with error bars for SNP and CNP films in dry air (▲) and exposed to Tol (■) and EtOH (●) vapors as indicated. Note that dry air was run as a background. UV–vis plots in panel a are offset for better comparison.

λ_{\max} to blue and red from 547 to 543 nm and from 551 to 559 nm, respectively, and barely responded to dry air over the entire run. Finally, the film returns close to its baseline ($\lambda_{\text{baseline}}$) after 450 s in dry air. Figure 1b also shows that the film needs some time to reach a maximum plasmon shift (180 s) and there is a plasmon fluctuation during vapor exposure. Since the film is exposed to headspace vapors, we believe the analyte needs time to partition into the organic film, to move through the alkane chains, and to reside nearby the surface to produce a significant change. It is also reasonable to think that nanoparticle mobility plays a direct role in the sensing mechanism. This could involve rearrangement or restructuring of the film during vapor exposure leading to constant changes in the plasmon coupling effects. Figure S2 (Supporting Information) compares a plot of maximum plasmon change (λ_{\max}) taken every 90 s over an extended period of time (15 min) for SNP and CNP films immersed in EtOH and Tol solvents. The figure shows that the plasmon response for SNPs also fluctuates over time. On the contrary, the CNP film shows a more stable plasmon shift over the entire run. At this point, the source of fluctuation observed for SNP films is uncertain. Future experiments will be designed to determine this more conclusively. Importantly, the plasmon shift follows a general trend toward either red or blue indicating film selectivity. Figure 1c shows a bar chart with the percent response (% R) from three devices along with quantitative statistical analysis based on changes in λ_{\max} for SNP and CNP films exposed to vapors as indicated. Percent response (% R) was calculated as follows:

$$\%R = [(\lambda_r - \lambda_b) / \lambda_b] \times 100\%$$

where λ_b is the plasmon baseline measured with the film in dry air and λ_r is the maximum plasmon response in the presence of vapor. Table S2 (Supporting Information) shows statistics for all the SNP and CNP devices involved in this study. Our results show a distinct shift to red (% R = 0.93) and blue (% R = -0.60) for SNP films upon EtOH and Tol vapors, respectively. There are three noticeable features in the chart. First, the SNP film blue shifts in the presence of Tol vapor. Second, SNP films are more responsive to EtOH than Tol vapor although the latter has a higher RI. Third, SNP films are ~3 times more sensitive than CNPs when exposed to EtOH vapors.

Changes to blue in LSPR vapor sensors have been rarely observed.²⁹ For instance, Rubinstein and co-workers prepared Au films coated with hydrophobic and hydrophilic polymers and exposed them to various vapor analytes including chloroform, Tol, water, and methanol.²⁹ They observed a blue plasmon shift in the presence of vapors that matched in polarity with the polymer film and suggested that the polymer swells, causing film thinning accompanied with a decrease in RI. Just a few groups associated plasmon changes with nanoparticle separation with plasmon changes since we cannot accurately predict the extension length of alkane chains upon vapor partitioning into the film. However, if we consider that each SNP is surrounded by a single TOABr monolayer, then the distance between two nanoparticles with fully extended TOA⁺ chains would be ~1.9 nm (0.12 nm for a single C–C bond).³⁷ Our TEM images (Figure S1, Supporting Information), consistent with other results,⁴⁶ indicate ~1.4 nm separation between Au nanoparticles. A distance shorter than 1.9 nm between nanoparticles is consistent with poorly organized alkane chains⁴¹ (vide infra) and some degree of interdigitatation.³⁷ Rechberger et al.²² observed a 1 nm blue plasmon shift

(λ_{\max}) for naked Au nanoparticles separated 0.9 nm and exposed to orthogonal polarized light. In view of their results and on the basis of our experimental blue shift $\lambda_{\max} = \sim -2.5$ nm, we estimate ~ 2.2 nm NP separation in the presence of Tol leading to ~ 3.6 nm total separation (1.4 initial + 2.2 nm swelling). A blue shift has also been attributed to film swelling in-plane with the substrate upon vapor exposure causing film thinning observed for Au²⁹ and Cu⁴⁷ islands coated with polymer films. Nevertheless, it is evident that nanoparticle separation and film thinning overcome the expected plasmon shift to red caused by Tol whose RI is higher than EtOH.

Film Swelling. To explore film morphology, we decided to expose a selected SNP film to Tol vapor.⁴⁸ Figure 2 shows an

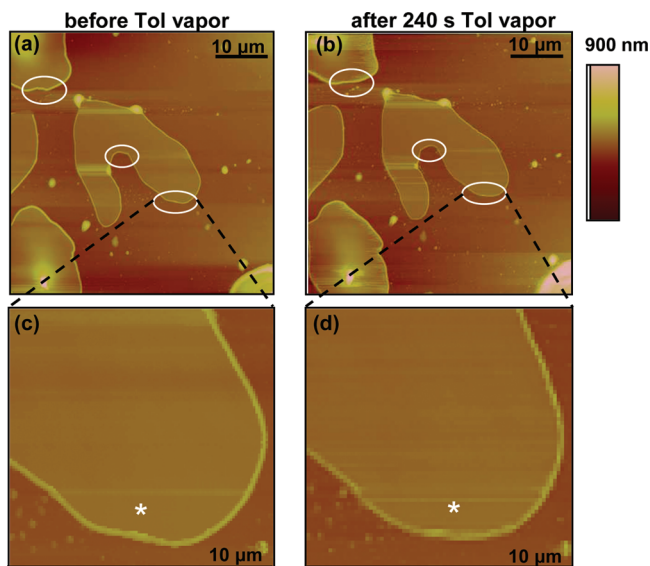


Figure 2. AFM image of a SNPs film on Si (100) before (a,c) and after (b,d) 240 s Tol exposure.

as-deposited SNP film on Si before and after exposure to Tol vapor for 240 s. The figure shows a nonhomogenous film comprised of some large and thick islands with remarkable bright borders and less crowded areas consistent with our SEM images (Figure S3, Supporting Information) and others.⁴³ The circles indicate areas where the film changed its structure to more rounded borders whereas average cross-section and root-mean-square roughness (w) show film changes after Tol vapor exposure. Cross sections were measured three times at the same spot (indicated with *) before and after Tol headspace vapor exposure. The w value was measured in three different areas at the central island shown in the figure. In the presence of Tol, the average film thickness and the average w value decreases from 141.0 to 115.3 nm and from 90.33 to 60.9 nm after Tol exposure, respectively.

Mie Theory and Film Compaction. The red shift is a common behavior when detecting changes with LSPR, but since the film may contract toward polar vapors, it is important to explore other possible contributions rather than the RI itself. The chart in Figure 1c showed a significant red shift for SNP films (% $R = 0.93$) as compared to CNP films (% $R = 0.30$) suggesting a different sensing mechanism. Figure 3a,b compares experimentally measured changes in the plasmon peak (λ_{\max}) vs the RI for similar size SNP and CNP nanoparticle films measured in air and exposed to vapor- and liquid-phase EtOH, respectively. As expected, SNP films exposed to liquids exhibit

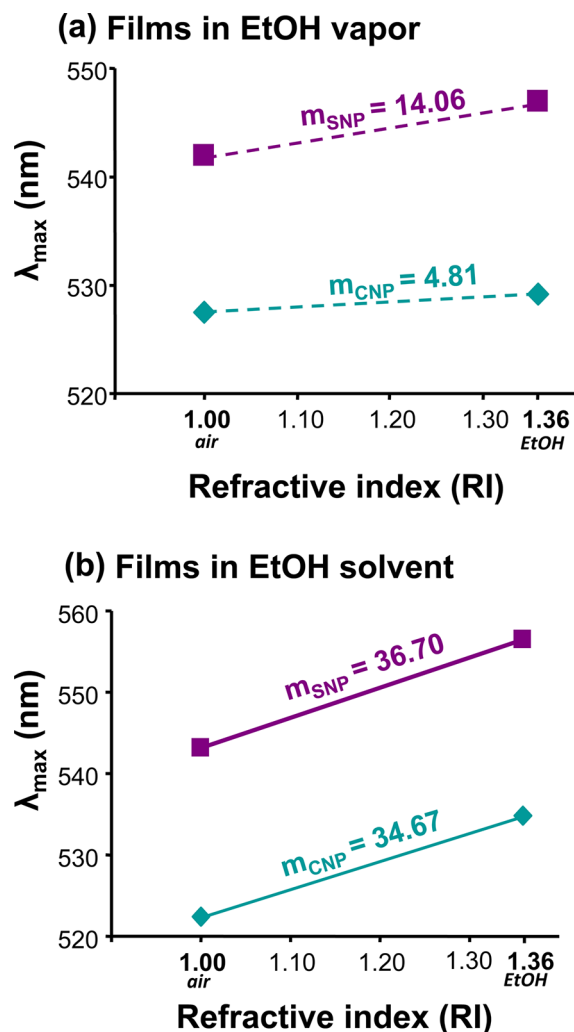


Figure 3. Experimentally measured maximum changes in the plasmon peak (λ_{\max}) with the refractive index (RI) for SNP (■) and CNP (◆) films exposed to air (dry air) and EtOH in vapor phase (a) and liquid phase (b).

higher sensitivity.⁴⁹ Surprisingly, the slope (m_{SNP}) for the organic-coated Au NPs is larger than the slope for weakly stabilized CNP films (m_{CNP}). These results are consistent with Figure 1c but fall off from the Mie's theory which indicates ~ 5 nm decrease in the plasmon shift for SNPs when compared to CNPs dispersed in EtOH (See Expected LSPR changes calculated by the Mie theory in SI, Supporting Information). Nevertheless, our experiments still show that SNP films are more responsive than CNP films in the presence of EtOH vapor, suggesting interparticle distance decrease (film compaction) that is known to shift to longer wavelengths.

To explore into the possibility of film contraction, we performed SEM imaging for as-prepared and water-containing SNP films. We choose water over ethanol considering its higher polarity and lower propensity to nanoparticle agglomeration.⁵⁰ The as-deposited SNP film shows concentric "o-rings" along the surface⁴³ attributed to micelle formation. Interestingly, the water-containing film shows the formation of fractal patterns with the appearance of uniform voids and some agglomeration observed at a higher magnification (see Figure S3, Supporting Information). The increase in void size with water indicates film compaction in some areas of the film, consistent with

irreversible crack formation³⁸ and interparticle distance decrease⁵¹ observed in the literature. Pileni and co-workers⁵¹ observed a distance decrease between C12S Au MPCs from 2.2 to ~1.1 nm by the addition of water. They suggested attractive forces caused between nanoparticles via water–water molecule interactions on the Au surface.

FT-IR Sensing. We now turn to the discussion of the organic coating and its effect on sensing. We performed FT-IR experiments to gain insights into the organic layer restructuring³⁹ by looking at changes in the asymmetric (d^-) CH_2 stretching vibrations.

Table 1 compares $d^- \text{CH}_2$ before ($t = 0$), during, and after analyte vapor exposure for selected SNP and C12 Au MPC

Table 1. Asymmetric (d^-) CH_2 Frequency Changes for Films of SNPs and C12S Au MPCs before (Dry Air), during, and after (Open to Ambient Air) Vapor Exposure

	SNP films		
	$d^- t = 0$ dry air	d^- vapor (max)	d^- open to ambient
EtOH	2923.46	2920.59	2922.96
Tol		2929.59	2923.28
	C12S Au MPC films		
	$d^- t = 0$ dry air	d^- vapor (max)	d^- open to ambient
EtOH	2917.63	2918.22	2918.49
Tol		2935.39	2918.81

films. A comparison between as-deposited SNP and C12S Au MPC films shows that CH_2 stretching for the former appears at higher frequency indicating higher density of gauche defects.⁴² Interestingly, C12S Au MPC films shift in EtOH vapor less prominently than SNP films and the opposite occurs in the presence of Tol. These data indicate that SNP and C12S Au MPC films are more sensitive to polar and nonpolar vapors, respectively, similar to chemiresistors composed of surfactant- and thiol-coated Au NP films.⁴³ We believe that polar vapors partition better on surfactant-coated nanoparticles than on strongly bound and well-organized alkanethiols causing larger film restructuring. Through these experiments, we can correlate film order with interparticle separation and predict consecutive changes in the LSPR sensor.

Figure 4a shows an actual FT-IR plot from a selected SNPs sample exposed to vapor analytes as indicated. Figure 4b shows a frequency shift for the $d^- \text{CH}_2$ versus time (s) for a selected SNP film exposed to EtOH and Tol vapors run in dry air (baseline) as indicated. The figure shows an increase in frequency for the film exposed to Tol while air and EtOH stay put and shift to a lower frequency, respectively. These results clearly demonstrate that the organic chains restructure in the presence of vapors, reach vapor saturation, and return to the baseline frequency after vapor removal (Table 1). We tested other vapors including hexane, acetone, butanol, isopropanol, methanol, and water as shown in Figure 5. The figure depicts the maximum frequency change (Δf_{max}) vs polarity for SNP films exposed to various vapor analytes as indicated. The bar chart shows average percent frequency response (avg. % R_f)⁵² along with the dielectric value (ϵ) from each vapor analyte involved in this study. Figure 5 demonstrates that changes in frequency cannot be solely attributed to changes in ϵ , rather it is a combination of different factors that may include vapor pressure, molecular shape (planar or linear), partition coefficient, polarity, and the presence or absence of aromatic

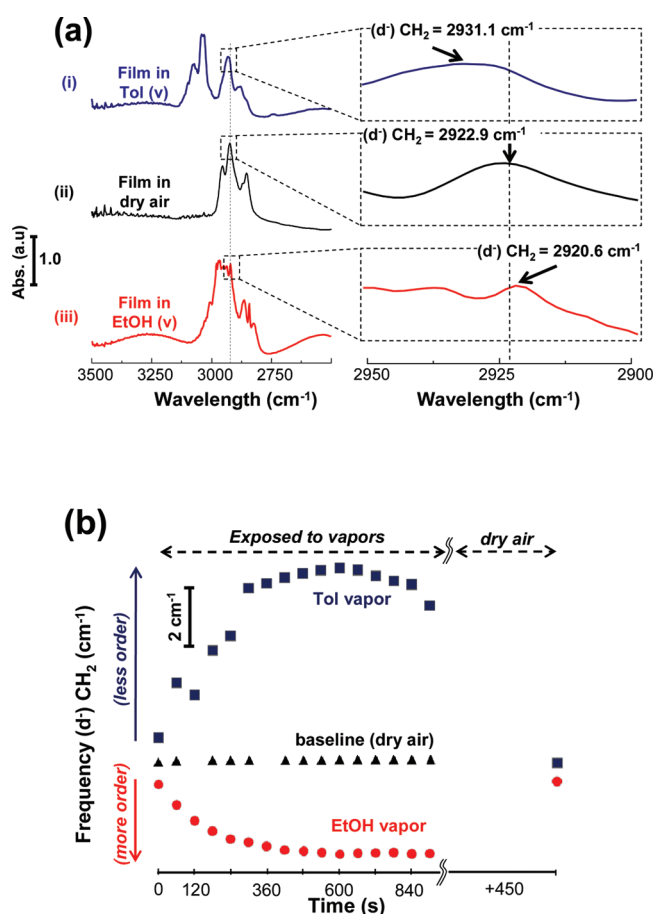


Figure 4. (a) FT-IR plots for an as-deposited SNP film in dry air (baseline or background gas, ii) and exposed to Tol (i) and EtOH (iii) vapors, and (b) the asymmetric (d^-) CH_2 stretching vibration from a selected SNP film at the indicated time.

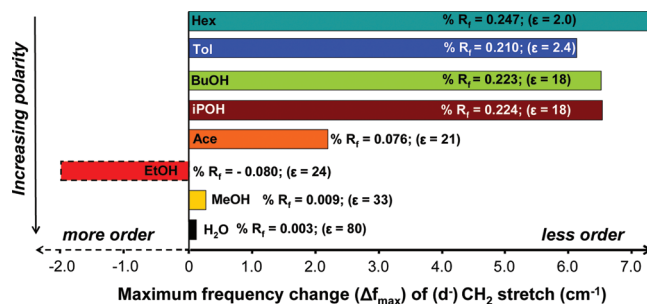


Figure 5. Maximum frequency change (Δf_{max}) for asymmetric CH_2 stretching vibration vs polarity obtained from 2 SNP films exposed to various VOCs as indicated. The bar chart shows average percent response (% R_f) and dielectric (ϵ) values. Note: Hex = hexane, Tol = toluene, BuOH = 1-butanol, iPOH = isopropanol, Ace = acetone, and EtOH = ethanol.

groups. Accordingly, SNP films exposed to EtOH behave distinctly by shifting toward a more organized state. These results may shine light on the importance of vapor solubility in the organic film. For instance, EtOH produces a distinct behavior when compared to a lower carbon chain vapor (i.e., methanol) suggesting that EtOH molecules have higher probability of reaching the Au surface leading to potential H-bonding formation. This may favor alkane chain packaging resulting in film compaction as observed in the literature⁵¹ and

by SEM images (See SI, Supporting Information). In general, films exposed to organic vapors respond with a shift toward lower energy indicating disorganization while, in the presence of vapors with relatively high dielectric (ϵ), the film either disorganizes to a lesser extent or responds with a shift toward higher energy (i.e., $\epsilon_{\text{EtOH}} = 24$). Organization can be attributed to van der Waals interactions between hydrocarbon chains caused by polar vapors while disorganization is associated with the degree of solubility between the analyte vapor and the organic material in the film.

Sensor Long-Term Stability. Table S3 (Supporting Information) and Figure 6 show the % response along with

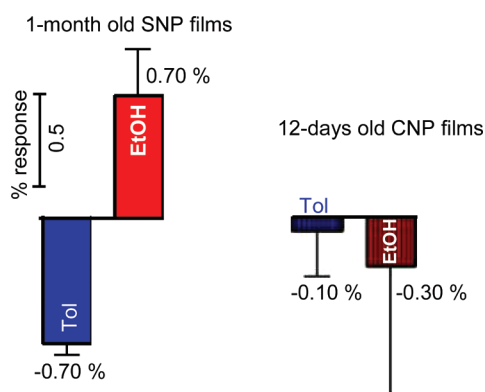


Figure 6. Bar chart showing % response and statistics for aged TOABr-coated Au and citrate-coated Au NPs exposed to Tol and EtOH vapors as indicated.

statistics for three SNP and CNP films stored at ambient conditions during 30 and 12 days, respectively. Interestingly, the one-month old SNP devices responded similarly to freshly prepared films but slightly improved their response from 0.6% to 0.7% upon Tol vapor. This increase in sensitivity falls within the standard deviation (STD) for the freshly-prepared samples (Figure 1c). CNP films, however, barely responded to the presence of vapors and in some cases shifted to blue indicating film deterioration. We also tried to compare stability between one-month old SNP and citrate-coated Ag nanoparticle films but Ag nanoparticles lost the plasmon band (Figure S4, Supporting Information).

CONCLUSIONS

In summary, a LSPR interparticle distance-based vapor sensing experiment with surfactant-coated Au NPs has now been demonstrated and compared with weak and strong ligands surrounding the nanoparticles. In the present work, the nanoparticle mobility in the film induced by the analyte vapor plays a crucial role in the LSPR sensing mechanism. The presence of Tol disorganizes the organic portion consistent with film swelling and nanoparticle separation. In LSPR, this has led to a competition between the expected red shift (caused by the increase in RI) and an overall predominating blue shift induced by film swelling. As expected, a red shift is observed when the SNP films are exposed to polar vapors although they respond more prominently than CNP films indicating cooperation between nanoparticle distance shrinkage and RI. We demonstrated that films containing water tend to film compaction and that polar vapors (i.e; EtOH) tend to organize the organic alkane chains. Importantly, the nanoparticle mobility in the film influences the LSPR changes over the

changes in the RI. Our results demonstrate that TOABr-Au solid-state films are easily assembled on transparent substrates, selective to polar and nonpolar vapors, more sensitive to LSPR sensor than citrate-coated Au nanoparticles, and more stable than citrate-coated Au and Ag NPs. Future experiments will explore the synthesis of TOABr-Ag and -Ag/Au alloy nanoparticles for keeping stability and improving sensitivity in LSPR sensors.

ASSOCIATED CONTENT

Supporting Information

Additional information as noted in text. This material is available free of charge via the Internet at <http://pubs.acs.org>.

AUTHOR INFORMATION

Corresponding Author

*E-mail: fjiban@inifta.unlp.edu.ar

Notes

The authors declare no competing financial interest.

ACKNOWLEDGMENTS

We gratefully acknowledge Agencia Nacional de Promoción Científica y Tecnológica for the following projects, PRH-74, PICT-PRH 295, and ANPCyT (PICT-2010-2554), and partial support from CONICET (PIP 0139). We also want to thank both Eugenia Zelaya (Centro Atómico Bariloche, CAB) and Gastón Corthey (INIFTA) who took the images and provided a great deal of help with TEM.

REFERENCES

- (1) Johnson, P. B.; Christy, R. W. *Phys. Rev. B* **1972**, *6*, 4370–4379.
- (2) Chen, H.; Kou, X.; Yang, Z.; Ni, W.; Wang, J. *Langmuir* **2008**, *24*, 5233–5237.
- (3) Haes, A. J.; Hall, W. P.; Chang, L.; Klein, W. L.; Van Duyne, R. P. *Nano Lett.* **2004**, *4*, 1029–1034.
- (4) Beeram, S. R.; Zamborini, F. P. *J. Am. Chem. Soc.* **2009**, *131*, 11689–11691.
- (5) Willets, K. A.; Van Duyne, R. P. *Annu. Rev. Phys. Chem.* **2007**, *58*, 267–297.
- (6) Mayer, K. M.; Hafner, J. H. *Chem. Rev.* **2011**, *111*, 3828–3857.
- (7) Satija, J.; Bharadwaj, R.; Sai, V. V. R.; Mukherji, S. *Dovepress* **2010**, 171–188.
- (8) Nath, N.; Chilkoti, A. *Anal. Chem.* **2004**, *76*, 5370–5378.
- (9) Sun, Y.; Xia, Y. *Anal. Chem.* **2002**, *74*, 5297–5305.
- (10) Mock, J. J.; Barbic, M.; Smith, D. R.; Schultz, D. A.; Schultz, S. J. *Chem. Phys.* **2002**, *116*, 6755–6759.
- (11) Link, M. A.; Mohamed, S.; El-Sayed, M. B. *J. Chem. Phys. B* **1999**, *103*, 3073–3077.
- (12) Henry, A.-I.; Bingham, J. M.; Ringe, E.; Marks, L. D.; Schatz, G. C.; Van Duyne, R. P. *J. Phys. Chem. C* **2011**, *115*, 9291–9305.
- (13) Kwon, M. J.; Lee, J.; Wark, A. W.; Lee, H. J. *Anal. Chem.* **2012**, *84*, 1702–1707.
- (14) Sau, T. K.; Murphy, C. J. *Langmuir* **2004**, *20*, 6414–6420.
- (15) Li, Z.; Tao, J.; Lu, X.; Zhu, Y.; Xia, Y. *Nano Lett.* **2008**, *8*, 3052–3055.
- (16) Hall, W. P.; Modica, J.; Anker, J.; Lin, Y.; Mrksich, M.; Van Duyne, R. P. *Nano Lett.* **2011**, *11*, 1098–1105.
- (17) Sannomiya, T.; Hafner, C.; Voros, J. *Nano Lett.* **2008**, *8*, 3450–3455.
- (18) Beeram, S. R.; Zamborini, F. P. *J. Phys. Chem. C* **2011**, *115*, 7364–7371.
- (19) Liz-Marzán, L. M.; Giersig, M.; Mulvaney, P. *Langmuir* **1996**, *12*, 4329–4335.
- (20) Jain, P. K.; Huang, W.; El-Sayed, M. A. *Nano Lett.* **2007**, *7*, 2080–2088.

- (21) Su, K.-H.; Wei, Q.-H.; Zhang, X.; Mock, J. J.; Smith, D. R.; Schultz, S. *Nano Lett.* **2003**, *3*, 1087–1090.
- (22) Rechberger, W.; Hohenau, A.; Leitner, A.; Krenn, J. R.; Lamprecht, B.; Aussenegg, F. R. *Opt. Commun.* **2003**, *220*, 137–141.
- (23) Agrawal, V. V.; Varghese, N.; Kulkarni, G. U.; Rao, C. N. R. *Langmuir* **2008**, *24*, 2494–2500.
- (24) Ni, I.-C.; Yang, S.-C.; Jiang, C.-W.; Luo, C.-S.; Kuo, W.; Lin, K.-J.; Tzeng, S.-D. *J. Phys. Chem. C* **2012**, *116*, 8095–8101.
- (25) Liu, N.; Tang, M. L.; Hentschel, M.; Giessen, H.; Alivisatos, A. P. *Nat. Mater.* **2011**, *10*, 631–636.
- (26) Bingham, J. M.; Anker, J. N.; Kreno, L. E.; Van Duyne, R. P. *J. Am. Chem. Soc.* **2010**, *132*, 17358–17359.
- (27) Chen, Y.-Q.; Lu, C.-J. *Sens. Actuators, B: Chem* **2009**, *135*, 492–498.
- (28) Chen, K.-J.; Lu, C.-J. *Talanta* **2010**, *81*, 1670–1675.
- (29) Karakouz, T.; Vaskevich, A.; Rubinstein, I. *J. Phys. Chem. B* **2008**, *112*, 14530–14538.
- (30) Malinsky, M. D.; Kelly, K. L.; Schatz, G. C.; Van Duyne, R. P. *J. Am. Chem. Soc.* **2001**, *123*, 1471–1482.
- (31) Cheng, C.-S.; Chen, Y.-Q.; Lu, C.-J. *Talanta* **2007**, *73*, 358–365.
- (32) Templeton, A. C.; Pietron, J. J.; Murray, R. W.; Mulvaney, P. J. *Phys. Chem. B* **1999**, *104*, 564–570.
- (33) Steinecker, W. H.; Rowe, M. P.; Zellers, E. T. *Anal. Chem.* **2007**, *79*, 4977–4986.
- (34) Ibañez, F. J.; Zamborini, F. P. *Small* **2012**, *8*, 174–202.
- (35) Wohltjen, H.; Snow, A. W. *Anal. Chem.* **1998**, *70*, 2856–2859.
- (36) Joseph, Y.; Guse, B.; Vossmeier, T.; Yasuda, A. *J. Phys. Chem. C* **2008**, *112*, 12507–12514.
- (37) Terrill, R. H.; Postlethwaite, T. A.; Chen, C.; Poon, C.-D.; Terzis, A.; Chen, A.; Hutchison, J. E.; Clark, M. R.; Wignall, G. J. *Am. Chem. Soc.* **1995**, *117*, 12537–12548.
- (38) García-Berrios, E.; Gao, T.; Woodka, M. D.; Maldonado, S.; Brunschwig, B. S.; Ellsworth, M. W.; Lewis, N. S. *J. Phys. Chem. C* **2010**, *114*, 21914–21920.
- (39) Snyder, R. G.; Strauss, H. L.; Elliger, C. A. *J. Phys. Chem.* **1982**, *86*, 5145–5150.
- (40) Hostetler, M. J.; Stokes, J. J.; Murray, R. W. *Langmuir* **1996**, *12*, 3604–3612.
- (41) Cheng, W.; Dong, S.; Wang, E. *Langmuir* **2003**, *19*, 9434–9439.
- (42) Grumelli, D.; Méndez De Leo, L. P.; Bonazzola, C.; Zamylyny, V.; Calvo, E. J.; Salvarezza, R. C. *Langmuir* **2010**, *26*, 8226–8232.
- (43) Ibañez, F. J.; Zamborini, F. P. *ACS Nano* **2008**, *2*, 1543–1552.
- (44) Murphy, C. J.; Sau, T. K.; Gole, A. M.; Orendorff, C. J.; Gao, J.; Gou, L.; Hunyadi, S. E.; Li, T. *J. Phys. Chem. B* **2005**, *109*, 13857–13870.
- (45) Brust, M.; Walker, M.; Bethell, D.; Schiffrin, D. J.; Whyman, R. J. *Chem. Soc., Chem. Commun.* **1994**, *7*, 801–802.
- (46) Fink, J.; Kiely, C. J.; Bethell, D.; Schiffrin, D. J. *Chem. Mater.* **1998**, *10*, 922–926.
- (47) Luechinger, N. A.; Loher, S.; Athanassiou, E. K.; Grass, R. N.; Stark, W. J. *Langmuir* **2007**, *23*, 3473–3477.
- (48) Ibañez, F. J.; Gowrishetty, U.; Crain, M. M.; Walsh, K. M.; Zamborini, F. P. *Anal. Chem.* **2005**, *78*, 753–761.
- (49) Thomas, K. G.; Zajicek, J.; Kamat, P. V. *Langmuir* **2002**, *18*, 3722–3727.
- (50) As observed in the Brust-Schiffrin cleaning procedure.
- (51) Salzemann, C.; Zhai, W.; Goubet, N.; Pileni, M.-P. *J. Phys. Chem. Lett.* **2009**, *1*, 149–154.
- (52) % Response (% R_f) = $[(f_r - f_b)/f_b] \times 100\%$, where f_r is the response frequency and f_b is the baseline frequency.